Advanced microstructure diagnostics and interface analysis of modern materials by high-resolution analytical transmission electron microscopy

W. NEUMANN*, H. KIRMSE, I. HÄUSLER, A. MOGILATENKO, CH. ZHENG, and W. HETABA

Institute of Physics, Humboldt University of Berlin, Newtonstrasse 15, 12489 Berlin, Germany

Abstract. Transmission electron microscopy (TEM) is a powerful diagnostic tool for the determination of structure/property relationships of materials. A comprehensive analysis of materials requires a combined use of a variety of complementary electron microscopical techniques of imaging, diffraction and spectroscopy at an atomic level of magnitude. The possibilities and limitations of quantitative TEM analysis will be demonstrated for interface studies of the following materials and materials systems: Nickel-based superalloy CMSX-10, $(Zn,Cd)O/ZnO/Al_2O_3$, $(Al,Ga)N/AlN/Al_2O_3$, $GaN/LiAlO_2$ and FeCo-based nanocrystalline alloys.

Key words: electron microscopy, energy dispersive X-ray spectroscopy, electron energy-loss spectroscopy, electron holography, Lorentz microscopy, interface analysis.

1. Introduction

Advances in materials science and engineering for the design of dedicated materials with tailored properties are connected with the comprehensive analysis of the microstructure and chemical composition of the materials and materials systems. The increasing use of micro- and nanoscale materials where the reduced dimensionality may drastically change the physical properties demands imaging and composition analysis with high spatial resolution for correlating the structure and properties of the materials investigated. Transmission electron microscopy (TEM) and scanning transmission electron microscopy (STEM) in combination with analytical methods allow a detailed insight into the materials characteristics. In order to correlate the structure, chemistry and physical properties of micro- and nanoscaled materials the various TEM techniques for imaging, diffraction and spectroscopy have to be combined. An overview of the main methods of TEM/STEM is given in Fig. 1.

The classical techniques of diffraction contrast imaging (bright-field (BF) imaging, dark-field (DF) imaging, weak-beam (WB) imaging) as routine methods of conventional TEM are applied to determine the nature and crystallography of crystal defects and interfaces. When investigating micro- and nanosized materials their size, shape and arrangement are determined using the diffraction contrast method, where a quantitative analysis often requires image simulations of diffraction contrast for theoretical structure models [1]. Investigating structure and composition of the materials of various size at an atomic scale high-resolution TEM (HRTEM) has to be applied. Due to the complexity of both, the scattering and the imaging process, the interpretation of HRTEM images also demands image simulations. Another way of structure re-

trieval is the determination of the scattered wave function at the exit surface of the crystalline specimen by electron holography or focus series reconstruction [2, 3]. Furthermore, various methods of quantitative HRTEM (qHRTEM) exist to determine the local strain and chemical composition on atomic scale [4].
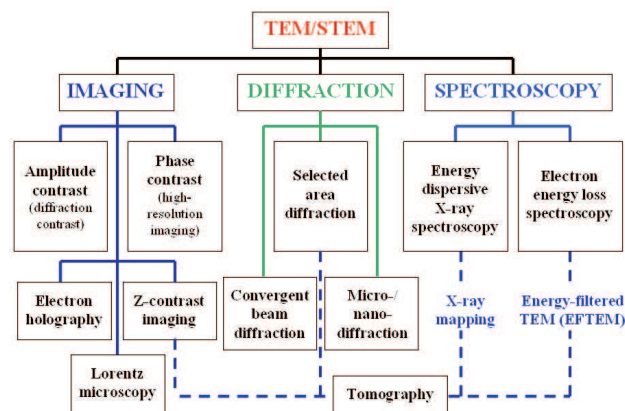

Fig. 1. Main methods of TEM/STEM

The methods of electron diffraction using a parallel or a convergent beam provide quantitative structural information of crystalline and non-crystalline materials. The classical parallel beam electron diffraction technique, i.e. selected-area electron diffraction, is commonly used to gain information about the degree of crystallinity of the materials as well as of basic parameters of crystal structure (e.g. lattice parameter, type of Bravais lattice) and specimen orientation. Due to the strong interaction between the electron beam and the crystal potential the intensities of the diffraction spots in a con-

*e-mail: wolfgang.neumann@physik.hu-berlin.de

W. Neumann, H. Kirmse, I. Häusler, A. Mogilatenko, Ch. Zheng, and W. Hetaba

ventional electron diffraction pattern obtained along a major zone axis are dynamically excited. Therefore, standard structure analysis methods as used in X-ray diffraction can only be applied when kinematical diffraction conditions are given (e.g. very thin crystals, crystal structures with at least one short axis). An extension for crystal structure analysis starting from electron diffraction intensities as input data is given by means of the precession electron diffraction technique, where the electron beam is rocking over the specimen generating a hollow cone illumination [5]. The convergent-beam electron diffraction (CBED) method provides information on the three-dimensional crystal structure and can therefore be applied to determine the point and space group of the material. CBED enables the precise measurement of the lattice parameters as well as the strain state of the crystalline material, where the large-angle convergent beam diffraction (LACBED) technique is very advantageous [6, 7]. Furthermore, CBED can be applied to determine the enantiomorphism and polarity of crystals. In order to study structural features and peculiarities of nanomaterials like nanowires, nanotubes, nanoclusters and precipitates the electron nanodiffraction method using both a nano-scale convergent or parallel beam mode can be used.

The main goal of analytical TEM (energy-dispersive X-ray spectroscopy (EDXS), electron energy-loss spectroscopy (EELS), energy-filtered TEM (EFTEM)) and STEM (Z-contrast imaging) is the quantitative determination of chemical composition. Dedicated nanoanalytical techniques can be applied to determine the element distribution along a line (X-ray line profile, series of EEL spectra) or in two dimensions (X-ray mapping, EFTEM). Additionally, EELS provides direct information on the local electronic structure of a material. The local chemical bonding can be determined by analysing the electron loss near edge fine structure (ELNES) and comparison with theoretical models. Chemical information on atomic scale can also be obtained using the STEM Z-contrast imaging technique, where a high-angle annular dark field (HAADF) detector is used for chemical imaging [8].

Lorentz microscopy and electron holography are very useful techniques for the evaluation of the structure of magnetic materials [2, 9, 10]. Additionally, electron holography can be used as an alternative and powerful method for the three-dimensional reconstruction of the shape of nanostructures from two-dimensional phase mapping.

In general, TEM images represent two-dimensional projections of a three-dimensional structure. In order to get a thorough understanding of the investigated three-dimensional object very often, particularly when dealing with nanomaterials, the exact knowledge of structure and composition in three dimensions is necessary. Various methods of electron tomography in materials science (HAADF-STEM, HRTEM, EDXS, EELS, EFTEM, electron holography) were developed to gain the desired information in 3-d from a set of 2d-projections [11].

In addition, it should be noted that the various quantitative methods in TEM concerning both imaging and spectroscopy have to be modified very often for the analysis of nanostructures with respect to their individual geometry.

2. Experimental results

The following examples of combined use of various TEM techniques of imaging, diffraction and spectroscopy should demonstrate the manifold possibilities for microstructure diagnostics and interface analysis of advanced materials.

2.1. Nickel-base superalloy (CMSX-10). Single crystal superalloys show excellent creep and fatigue properties at high temperatures and are widely used as structure materials in gas turbines, e.g. as turbine blade material. Nickel-based single crystal superalloys consist of ordered cuboidal Ni_3Al precipitates (γ'-phase) and the fcc nickel solid solution matrix (γ-phase). The coexistence of γ-matrix and γ'-precipitates is controlled by heat treatment of the solution and the cooling rate. The analytically determined compositions of the two phases (γ and γ') of CMSX-10 using EDXS analysis are listed in Tab. 1. The substitution of the Ni atoms of Ni_3Al by Co, Al, Ti, Ta, Nb, Mo and W determines elastic and plastic properties as well as creep behaviour. Under mechanical load a directional coarsening of the γ'-precipitates occurs, generally denoted as rafting. This morphological change depends on many factors such as, e.g., the initial microstructure, the rate and temperature of deformation, and the γ/γ' misfit. In order to understand the diffusion processes during rafting the undeformed superalloy after a heat treatment has to be analysed.

Table 1
Element concentrations of the γ-matrix and γ'-precipitates determined by EDXS. $\overline{Z}$ is the average atomic number of the respective phase

	Al at.% Z = 13	Cr at.% Z = 24	Co at.% Z = 27	Ni at.% Z = 28	Ta at.% Z = 73	W at.% Z = 74	Re at.% Z = 75	$\overline{Z}$
γ	8.0	7.0	7.1	68.2	1.7	1.4	6.6	31
γ'	27.2	1.3	1.8	65.3	3.3	0.8	0.3	26

In Fig. 2 results of the analysis of the microstructure of CMSX-10 are given. Figure 2a shows an absorption contrast image of the specimen viewed along the [100] zone axis. The intensity of such images is influenced by both, the scattering efficiency of the material which depends on the mean atomic number and by the thickness of the TEM specimen. In both cases an inverse correlation with the intensity is found.
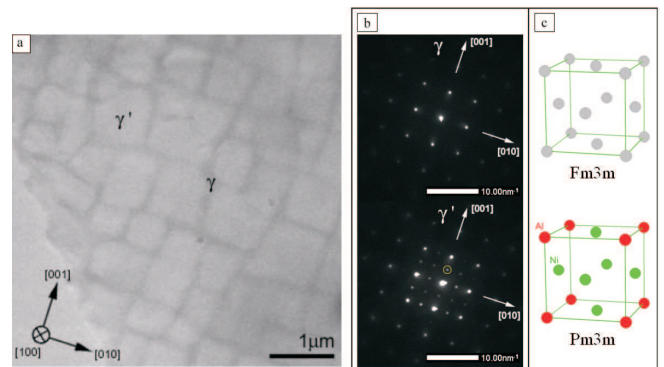

Fig. 2. Structure analysis of nickel-base superalloy (CMSX-10): a) TEM absorption contrast image, b) SAED patterns of the γ- and γ'-phases, c) corresponding structure models

Two phases can be recognized from their brightness in Fig. 2a. The γ'-phase forms bright rectangular shaped areas. Presuming constant thickness the high brightness hints to a lower mean atomic number of this phase. This is confirmed by the corresponding value for γ' which is lower than that for γ as given in Tab. 1. The bright rectangles or even squares of the γ'-phase have edge lengths ranging from 500 nm to 1 μm. These patterns are cross sections of the γ'-precipitates embedded in the γ matrix. In general, the edges of the precipitates are oriented along the $\langle 100 \rangle$ directions. The volume fraction of the γ'-phase amounts to about 80%. For determining the orientation relationship between the precipitates and the matrix selected area electron diffraction (SAED) was applied. Parallel alignment of the γ'- and γ-lattice (same azimuthal orientation) justifies the classification of CMSX-10 as a single crystal superalloy. From the SAED patterns the crystal structure type of both constituents was analysed. The main difference between both is evident from the additional weak reflections of the γ'-phase. One of the reflections is exemplarily encircled in Fig. 2b. These additional spots are caused by the transition from statistical occupancy of the lattice sites in the γ-phase (cf. Fig. 2c) to an ordered arrangement of the Ni and Al atoms in the cubic unit cell of the γ'-phase (symmetry reduction from F- to P-lattice). In general, the determination of the lattice parameters of the two phases with high precession is carried out by means of CBED. However, the SAED patterns can also be used for lattice parameter measurements as demonstrated in Fig. 3. On the one hand the SAED analysis suffers from larger error bars and limited lateral resolution but on the other hand the lattice parameters can easily be evaluated when comparing the experimental data with diffraction patterns of standard materials like GaAs. For the quantification of the lattice constants the reciprocal distance of the diffraction spots was determined from intensity profiles taken across the diffraction patterns of Fig. 2b along the [010] and [001] directions. Fig. 3a shows the profiles and the results of lattice constant calculations utilizing the following equation:

$$a = \frac{\sqrt{h^2 + k^2 + l^2}}{\left| \vec{g}_{hkl} \right|}.$$

This analysis proves the cubic structure of the γ'-phase with a lattice parameter of about $a'_{010} = a'_{001} = (0.3723 \pm 0.0016)$ nm. The lattice parameter of the γ-phase parallel to the precipitate walls perfectly matches to it. This shows that the phase separation starts from a perfect lattice. In contrast to that, the lattice parameter measured normal to the γ/γ' interface is larger ($a_{010} = (0.3806 \pm 0.0016)$ nm). Obviously, the matrix consists of tetragonal distorted unit cells. The sketch of Fig. 3b illustrates this arrangement of cubic and tetragonally distorted lattices.

This fact is well known also from other Ni-based superalloys (e.g. SC16), where the lattice parameters were also determined by X-ray diffraction measurements [12]. In addition, the lattice deformation was verified by quantitative HRTEM (see Fig. 4). This analysis permits the evaluation of elastic strain at a nanometer scale whereas SAED only allows an average determination of the lattice deformation over a few 100 nm. Figure 4a shows a Fourier-filtered HRTEM image of the γ/γ' interface region viewed along the [100] zone axis. Comparing the patterns of both phases the ordering of the γ'-phase can easily be recognized. The lattice deformation was evaluated down to the sub-angstrom level utilizing the peak finding method DALI (Digital Analysis of Lattice Images) [13]. For the strain analysis the displacement $\vec{u}_{001}$ was analysed along the [001] direction as indicated in Fig. 4a.
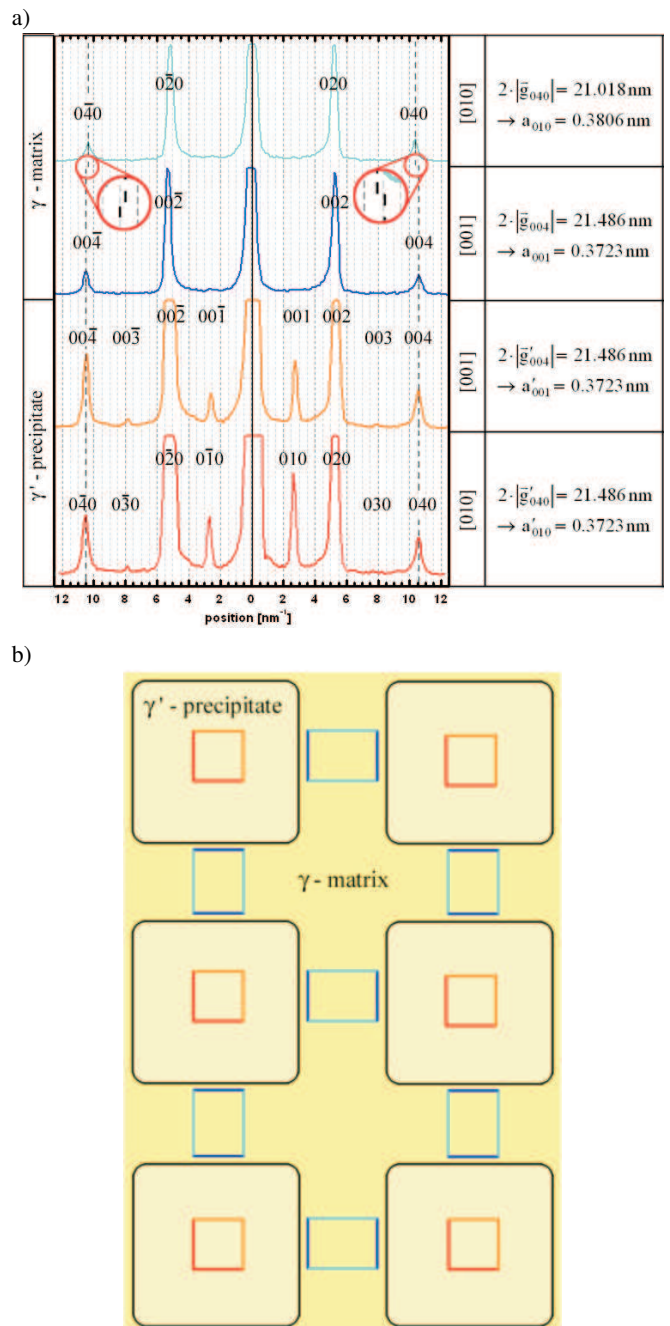
a)

b)

Fig. 3. Interpretation of the diffraction patterns (Fig. 2b): a) intensity profiles of the reflections along the [010] and [001] directions. The measured $\vec{g}$ vectors and calculated lattice parameter a are listed in the table, b) schematic presentation of arrangement and strain state of the unit cells
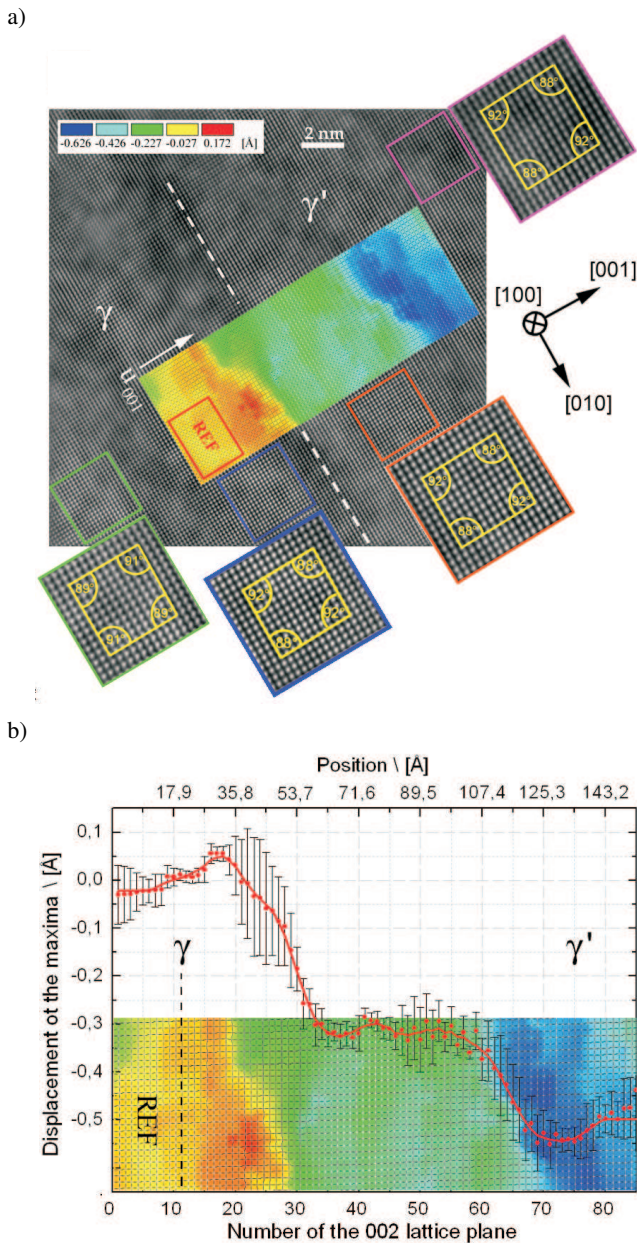
a)

b)

Fig. 4. Quantitative HRTEM of nickel-base superalloy (CMSX-10): a) Fourier-filtered HRTEM image of γ/γ' interface analysed by DALI. The colour-coded map represents the displacement of the atom columns in [001] direction compared to the reference lattice (REF), b) one-dimensional plot of displacements u_{001} of the (002) lattice planes with respect to the REF given in a). The values are averaged along the (002) lattice planes

As visualised by the superimposed colour coded map the displacement $\vec{u}_{001}$ reveals a gradient of the (002) lattice plane distance across the γ/γ' interface. The interface is marked by the dashed line. Starting from the reference area marked by REF the distance of the (002) lattice planes increases as indicated by the change of colour from yellow for the reference area to orange. As revealed by SAED the average γ-phase (matrix) is tetragonal distorted. The qHRTEM analysis shows that the lattice is additionally deformed near the γ/γ' interface. This is a consequence of the smaller lattice distance of the

γ'-phase. The lattices of both phases can only adapt to each other when the lattice of the γ-phase is compressed parallel to the interface. By this, a dilatation normal to the interface is forced. Consequently, the distance of the (002) lattice plane increases. Approaching the interface, the (002) lattice plane distance decreases as indicated by the transition from red to green. Further on, the distance remains constant as represented by the green colour within a region of 5 to 10 nm in width. Here, an equilibrium state between compression of the γ- and dilatation of the γ'-phase is found. Consecutively, the colour turns from green to blue. Compared to the γ-phase the equilibrium cubic lattice distance is smaller for the γ'-phase. In order to adapt both lattices, the lattice distance parallel to the interface has to be expanded. Consequently, the distance of the (002) lattice planes measured normal to the interface decreases significantly. Finally, the transition from dark blue to light blue is seen. This can be regarded as the transition from the strained to the unstrained lattice of the cubic γ'-phase.

In Fig. 4b the displacement of the atom columns along the [001] direction is plotted for the same region as analysed in Fig. 4a. The error bars are calculated by averaging the displacement values parallel to the γ/γ' interface. The red line exactly reproduces the displacement behaviour described above.

Carefully inspecting the HRTEM patterns of both phases, a distortion of the angles between the basis vectors of the $\langle 100 \rangle$ directions is found. In the magnified views inserted in Fig. 4a the measured angles are denoted. The deviation from the 90° angle of the unstrained cubic system is significant and amounts to about $\pm 2°$. The distortion is correlated with the strain between the two phases. For the γ-phase the distortion is reduced in a larger distance from the γ/γ' interface. A stronger distortion can be expected close to the edges of the precipitates. Here the lattice symmetry might be further reduced down to triclinic.

For the inspection of the distribution of the different atomic species on the atomic scale the chemically sensitive HAADF imaging technique was applied. The results are presented in Fig. 5. For gaining an overview of the specimen an image at low magnification was recorded (see Fig. 5a). The two phases can be clearly differentiated from their brightness. Due to the higher mean atomic number the γ-phase (matrix) appears brighter than the γ'-phase (precipitates). The decrease of the HAADF background intensity from upper left to lower right is due to the thickness gradient introduced by the TEM specimen preparation. The thinnest area of the specimen is visible at the lower right.

The high-resolution HAADF image of γ/γ' interface in Fig. 5b was taken with a TEM/STEM JEOL JEM 2200FS (200 kV) equipped with a FEG and a HAADF detector. Utilizing the minimum probe size of 0.14 nm enabled the spatial resolution of the atomic columns viewed along the [100] direction. These columns are separated by only 0.18 nm. Inspecting Fig. 5b the two phases are recognized. The bright dots in the γ'-phase are due to atomic columns containing one or more heavy atoms (e.g. Ta, W, Re). To gain more detailed information on the distribution of the bright spots the

capabilities of an STEM probe C_s corrected TEM/STEM JE-OL JEM 2100F/C_s corrector (FEG, 200 kV) were explored. The corresponding high-resolution HAADF image is given in Fig. 5c. The comparison of both images clearly reveals the improvement of the spatial resolution as well as of the HAADF image contrast. The progress provided by state-of-the-art instrumentation can be visualised more clearly by intensity profiles along the {001} lattice planes. The representative intensity profiles of both images are given. The path of the line scans is marked in the individual HAADF images (Fig. 5b and 5c). The profile of the HAADF image recorded with the uncorrected instrument exhibits a low signal-to-noise ratio. Moreover the individual atomic columns can hardly be recognized. On the contrary, the intensity profile of the image acquired with the probe C_s corrected microscope yields a high signal-to-noise ratio and a sinusoidal modulation of the intensity along the path permitting the direct correlation with the atomic columns. Hence, it is justified to conclude that the highest peak is correlated with an atomic column of the highest mean atomic number. For a direct determination of the chemical composition of the columns the analytical methods of EDXS or EELS have to be applied additionally.
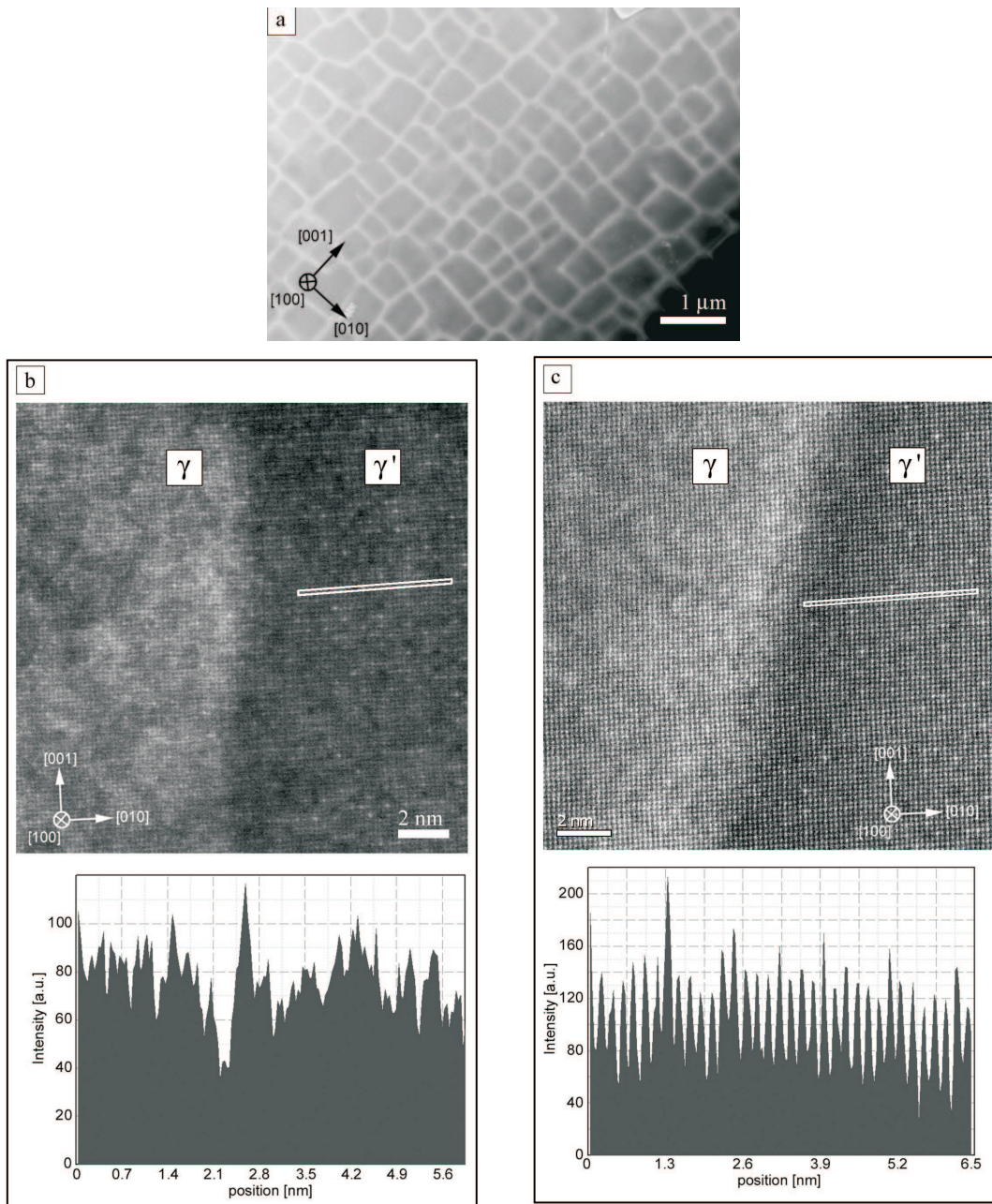

Fig. 5. HAADF imaging of nickel-base superalloy (CMSX-10): a) HAADF overview image, b) conventional high-resolution HAADF image (TEM/STEM JEOL JEM 2200FS (FEG, 200 kV, probe size: 0.14 nm)) of the γ/γ' interface and intensity profile along the marked line, c) C_s-corrected high-resolution HAADF image (TEM/STEM JEOL 2100F/C_s-corrector (FEG, 200 kV, probe size: 0.1 nm)) of γ/γ' interface and intensity profile along the marked line

2.2. (Zn,Cd)O/ZnO. The chemical abruptness of interfaces is an important parameter for the performance and life time of potential device structures. The materials system (Zn,Cd)O/ZnO is of particular interest for inorganic-organic hybrid semiconductor devices [14]. The Cd content of ternary (Zn,Cd)O allows to tune the band gap from UV- to near-infrared spectral range. Since the ternary layer is embedded in ZnO, the diffusion of Cd into ZnO limits the Cd content of the region near to the interface between the ternary and the binary layer as well as the abruptness of the (Zn,Cd)O/ZnO interface. The key parameter describing the diffusion process is the Cd diffusion constant D_0 in ZnO.

a)

b)
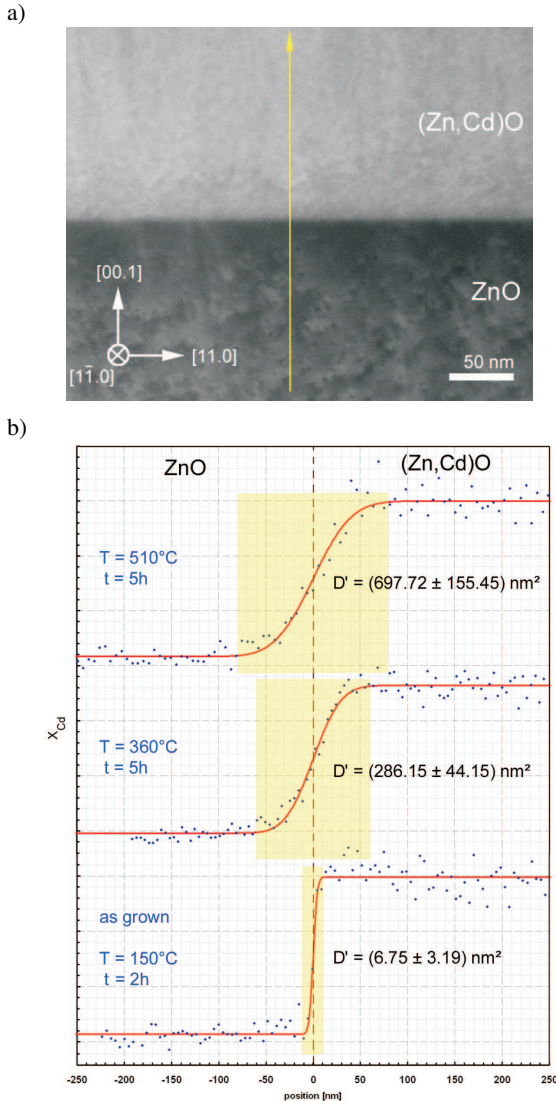
Fig. 6. Composition profiling of the (Zn,Cd)O/ZnO interface of three specimens after thermal annealing: a) high angle annular dark-field image of the as grown specimen ($T = 150°C$, $t = 2$ h). The arrow indicates the EDXS line scan across the interface, b) Cd concentration profiles across the interface of the 3 specimens (1st: $T = 150°C$, $t = 2$ h; 2nd: $T = 360°C$, $t = 5$ h; 3d: $T = 510°C$, $t = 5$ h). The evaluated "time dependent" Cd diffusion coefficients D' of Cd in ZnO along [00.1] direction are given. The dashed line corresponds to the Matano plane (position $x = 0$ nm) which is the initial position of the interface

In order to quantify the diffusion process three specimens, all differently thermally treated, were investigated. The first specimen is an as-grown one which was kept at 150°C for 2 h during the growth process of the 200 nm-thick (Zn,Cd)O cap layer. After the growth the second and third specimens were annealed for 5 h at 360°C and at 510°C, respectively.

EDXS line scans across the (Zn,Cd)O/ZnO interface of the differently annealed samples were acquired. A HAADF image of the as-grown specimen is shown in Fig. 6a. The transition of the image intensity from the ZnO (dark/bottom) to (Zn,Cd)O (bright/top) is due to the different mean atomic number of both components. The replacement of atomic positions of Zn by Cd increases the mean atomic number. Consequently, the (Zn,Cd)O layer appears brighter. The arrow in Fig. 6a indicates both, the length of the EDXS line scan and its orientation perpendicular to the (Zn,Cd)O/ZnO interface.

The results of the line scans acquired for the three samples are shown in Fig. 6b. The Cd concentration was quantified from the individual EDX spectra of each measuring point across the interfaces. In all cases the normalized Cd content is plotted linearly as a function of position. The parameters of the three different profiles are the annealing temperature T and the annealing time t. The dots represent the Cd content whereas the solid lines correspond to least square fits according to the error function applied to mathematical description of diffusion processes. The error function is given as follows:

$$y(x) = A \cdot erf\left(-\frac{x}{\sqrt{4 \cdot D'}}\right) \qquad (1)$$

with

$$D' = D \cdot t. \qquad (2)$$

Free parameters of this function are A and D'. A indicates the dilation of the error function along the y-axis which corresponds to the Cd content of the (Zn,Cd)O layer, whereas D' is a representative of the diffusion process. In Fig. 6b these values of D' are given for the three specimens. But, D' itself depends on two parameters, the diffusion coefficient D and the annealing time t. In general, the diffusion coefficient D is a tensor because the diffusion process depends on the crystal structure and the crystallographic directions. Additionally, D depends on the annealing temperature T, the diffusing atom species, and the chemical potential. The following Arrhenius equation characterises the diffusion:

$$D = D_0 \cdot \exp\left(-\frac{E}{k \cdot T}\right). \qquad (3)$$

For the diffusion in a crystalline material the atoms have to overcome an energy barrier E which is a characteristic of the material. By this, the atoms can move thermally activated from one lattice site to the next. At high temperatures this process is more likely than at low temperatures. D_0 is the extrapolated value of the diffusion coefficient D for an infinite annealing temperature and k is the Boltzmann constant. In the present case, D_0 quantifies the diffusion process of Cd atoms in ZnO along the [00.1] direction. For the determination of D_0 an Arrhenius plot is drawn in Fig. 7. Here, the values

of *ln(D)* are plotted as a function of the reciprocal annealing temperature T. The D values are independent of the annealing time as they were calculated by Eq. (2) using D' and t as given in Fig. 6b.
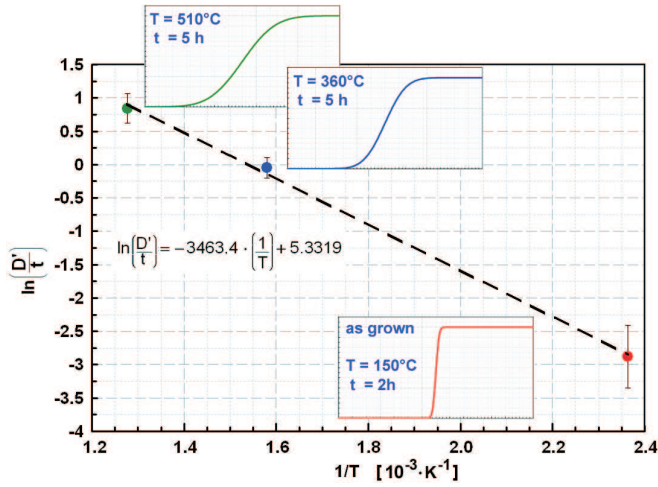

Fig. 7. Arrhenius plot of the diffusion coefficient D as a function of temperature. The dots are calculated from the corresponding Cd concentration profiles and annealing parameters (see images in rectangles). The dashed line is gained by linear regression

Equation (3) contains the two unknown parameters D_0 and E. Both can be determined by the logarithmic calculus of Eq. (3). Thus, one gets the following linear equation with $1/T$ as axis of abscissa:

$$\ln D = -\left(\frac{E}{k}\right) \cdot \frac{1}{T} + \ln D_0. \qquad (4)$$

Figure 7 shows the data points $\ln(D) = f(T^{-1})$ with the corresponding error bars and the calculated linear regression (dashed line). The following functional equation was received:

$$\ln D = -3463.9 \frac{\text{nm}^2 \cdot \text{K}}{\text{min}} \cdot \frac{1}{T[\text{K}]} + 5.33 \frac{\text{nm}^2}{\text{min}}. \qquad (5)$$

The intersection of this function and the axis of ordinate corresponds to $\ln(D_0)$. According to this evaluation the diffusion constant D_0 of Cd in ZnO along the [00.1] direction amounts to:

$$D = (206.44 \pm 1.30)\frac{\text{nm}^2}{\text{min}} = (3.55 \pm 0.02) \cdot 10^{-14} \frac{\text{cm}^2}{\text{s}}. \qquad (6)$$

Knowing this number, valuable conclusions can be drawn for the growth process of (Zn,Cd)O/ZnO heterostructures. Assuming an optimum growth temperature for two-dimensional growth, the duration of the growth of subsequent layers must not exceed a certain value. Otherwise layers of an intended thickness of only a few nanometres will disappear due to the diffusion of Cd out of (Zn,Cd)O into the adjacent ZnO.

2.3. (Al,Ga)N/AlN/Al$_2$O$_3$. Group-III wurtzite nitride semiconductors have been intensively analysed and successfully used for light-emitting device application since years. Recently, (Al,Ga)N alloys have been investigated for the application in deep-ultraviolet (UV) light-emitting diodes and laser diodes. Fabrication of high-efficiency (Al,Ga)N-based devices operating in the UV-range requires a combination of thick AlN buffer layer with (Al,Ga)N/AlN superlattices (SL) acting as dislocation stopping barriers. Growth of such structures is a challenging task, since the lattice misfit between sapphire substrates and AlN buffers as well as between AlN and (Al,Ga)N usually results in formation of a huge dislocation density. Decrease of dislocation densities is extremely important since it allows a considerable improvement of the device performance.

X-ray diffractometry is often used to estimate defect densities in thin layers. In this case the dislocation density can be calculated out of the full width at half maximum values of certain diffraction reflections [15]. However, this analysis averages over the whole thickness of thin films and does not account for possible inhomogeneities in the defect densities through the layers. In contrast, TEM allows a direct insight into the layer structure and can clearly show changes in the defect densities across the layer thickness and allows to distinguish between different types of defects.

Three types of perfect dislocations are known in the wurtzite nitride structure: screw dislocations with the Burgers vector $\vec{b} = <00.1>$, edge dislocations with $\vec{b} = 1/3 <11.0>$ and mixed dislocations with $\vec{b} = 1/3 <11.3>$. These defects can be distinguished in TEM using diffraction contrast imaging.

To acquire an image with a considerable diffraction contrast the sample is tilted out of zone-axis to a so-called two-beam condition, the condition in which only two beams appear in diffraction plane: the undiffracted beam and only one strongly exited beam *hkl*. When only the strongly diffracted *hkl* beam is used for the imaging one obtains the so-called dark-field image. At these conditions high image intensity appears only in the sample regions where the exact Bragg condition for the (*hkl*) planes is satisfied. If defects are present in the sample the lattice planes are locally strained around them, so that the exact Bragg condition can be satisfied only in a very narrow region next to the defect. As result the defect position is clearly visible since this region appears bright on the darker background (e.g. Fig. 8).

To distinguish between the dislocations of different character the so-called invisibility criterion is used. It states that a dislocation is invisible when the reciprocal lattice vector $\vec{g}_{hkl}$ characterising the imaging reflection *hkl* is perpendicular to the dislocation Burgers vector $\vec{b}$, i.e. $\vec{g} \cdot \vec{b} = 0$ for $\vec{g} \perp \vec{b}$. When $\vec{g} \| \vec{b}$ the dislocation is visible with a maximal contrast ($\vec{g} \cdot \vec{b} = \max$). However, it should be noted that this criterion is strictly valid for pure srew dislocations. For edge dislocations as well as partial dislocations additional parameters (e.g. additional displacement parallel to dislocation line) should be considered [16].

As an example Fig. 8 shows two dark-field images of an AlN layer grown on an Al$_2$O$_3$ substrate by MOCVD. The images were obtained using two different AlN reflections: 0002 and 11-20. They show different types of threading dislocations: the screw dislocations are visible in Fig. 8a and the

edge dislocations in Fig. 8b. Dislocations of the mixed character appear in both images, since their Burgers vector contains two components aligned along both [00.1] and [11.0] directions, as $1/3[11.3] = 1/3[11.0] + [00.1]$. From the dark-field images it is obvious that the dislocation density is not uniform through the AlN layer. The first 100 nm of AlN (see the dashed line in Fig. 8a) contain a huge number of dislocations. However, a large part of them annihilate as the layer thickness exceeds 100 nm. Additionally, some screw and mixed dislocations annihilate during the further growth of the layer (marked by dashed arrows).
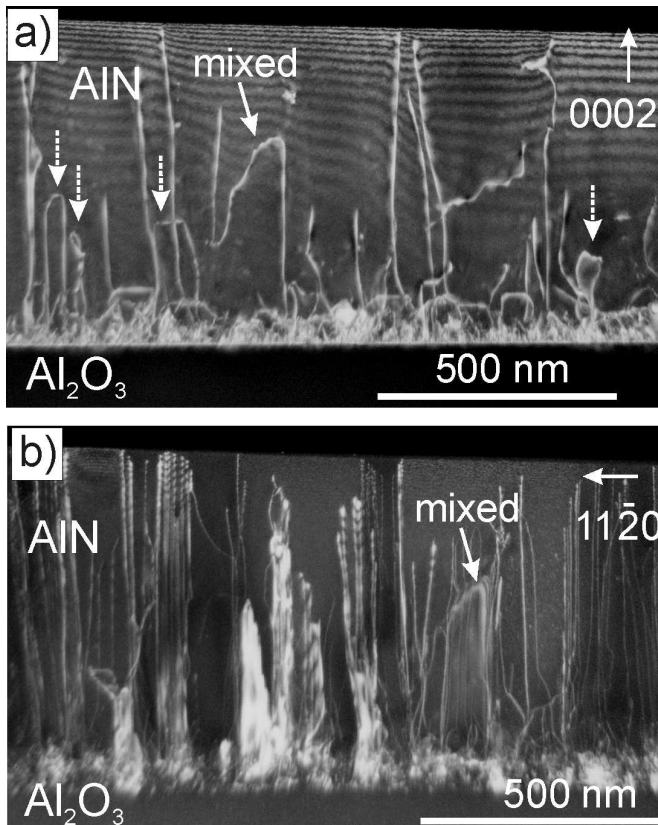
Fig. 8. Cross-sectional dark-field images of approximately the same specimen area obtained under two-beam diffraction conditions using a) g = 0002 and b) g = 11-20. The images show a) screw and b) edge dislocations. Dislocations with a mixed character are visible in both images. Dashed arrows in a) show annihilation of some dislocations with a screw component of the Burgers vector

From the dark-field images in Fig. 8 the screw and edge dislocation densities at the layer surface were calculated to be 5×10^9 cm^{-2} and 3×10^{10} cm^{-2}, correspondingly [17]. For this analysis the specimen thickness at the layer surface was estimated using a thickness fringe contrast.

It is also possible to visualize defects using annular dark-field detector (ADF) in STEM imaging mode. For this analysis a ring-shaped ADF detector have to be centred at the microscope optic axis. This means that all diffraction reflections from a certain scattering angle will contribute to the image formation. As result the obtained image will contain the contribution from diffraction contrast, so that the strain contrast around the dislocation lines will be clearly visible. Figure 9 shows an ADF image of a 30x AlN/(Al,Ga)N superlattice grown on a thick AlN buffer layer. The purpose of using the superlattice was to introduce an additional strain into the system in order to bend the dislocation lines and cause them to annihilate, which would result in a defect reduction in the sample. It is obvious that the strain introduced by the shown superlattice slightly bends the dislocation lines. However no dislocation reduction is observed.
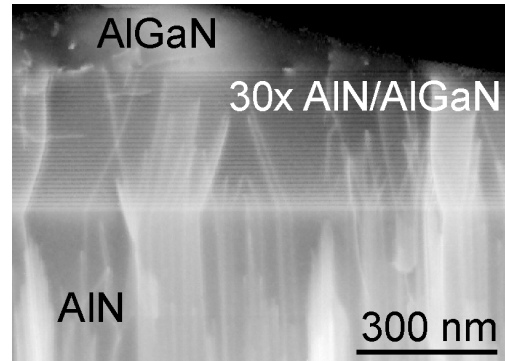

Fig. 9. Cross-sectional ADF STEM image of AlN/(Al,Ga)N superlattice grown on AlN buffer layer. Threading dislocations of all types (screw, edge, mixed) are visible as bright lines

The advantage of the ADF technique compared to the conventional dark-field imaging is its simplicity and possibility to visualize the defects with a considerable contrast already in zone axis. However, in ADF images dislocations of different types can not be distinguished from each other. Thus, this analysis can be used only if qualitative information is required, e.g. if there are any defects or if there is a reduction of dislocation density.

Basal plane stacking faults (BSF) were often observed in thin AlN layers of the AlN/(Al,Ga)N superlattices. Three types of BSF are known in the wurtzite structure [18]: two intrinsic stacking faults (I_1 and I_2) and one extrinsic stacking fault (E). Different types of BSF correspond to a different number of biatomic Al-N planes forming a cubic stacking (which is ...ABCABC...) in the hexagonal stacking sequence (which is ...ABABAB...), i.e. 3 planes for I_1 (ABAB__ABCBCBC__), 4 planes for I_2 (ABAB__ABCA__CACA) and 5 planes for E (ABAB__ABCAB__ABAB). Using HRTEM imaging it is possible to visualise the number of these planes and thus to determine the BSF type. Figure 10 shows an exemplary HRTEM image of an about 2 nm thick AlN layer in the AlN/(Al,Ga)N superlattice. An inset of Fig. 10 shows a Fourier filtered magnified image with a marked position of one additional biatomic Al-N plane in the wurtzite AlN structure. Thus the observed stacking fault represents the stacking sequence ...AB__ABC__BC..., which corresponds to I_1 stacking fault type. BSF I_1 is formed by removal of a basal plane followed by a slip of a crystal by $1/3 < 1\bar{1}.0 >$. This procedure can be described by a displacement vector $\vec{R} = 1/2[00.1] + 1/3 < 1\bar{1}.0 >$. The I_1 type stacking fault structure has the lowest formation energy compared to the other BSF [19].
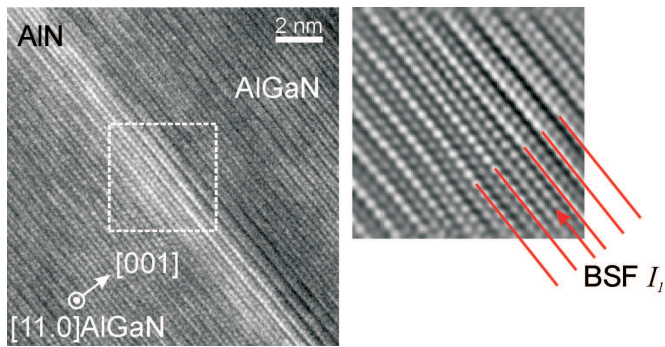
Fig. 10. HRTEM image of a thin AlN layer in an AlN/(Al,Ga)N superalttice with a Fourier filtered fragment showing periodic image of the wurtzite crystal structure (...ABAB...) containing an I_1 type basal plane stacking fault (...AB<u>ABC</u>BC...)

EDXS analysis has been carried out to check homogeneity of the layers and a possible intermixing at the interfaces. Figure 11a shows an elemental distribution of Al and Ga obtained from a quantified EDX signal acquired across the interface between the thick AlN buffer layer and a few first AlN/(Al,Ga)N superlattice layers. The line scan direction is shown in the corresponding HAADF STEM image by an arrow (Fig. 11b). Already from the Z-contrast HAADF image intensity it is visible that there is a certain intermixture at the interface between the AlN buffer and the AlN/(Al,Ga)N superlattice layers (Fig. 11b).
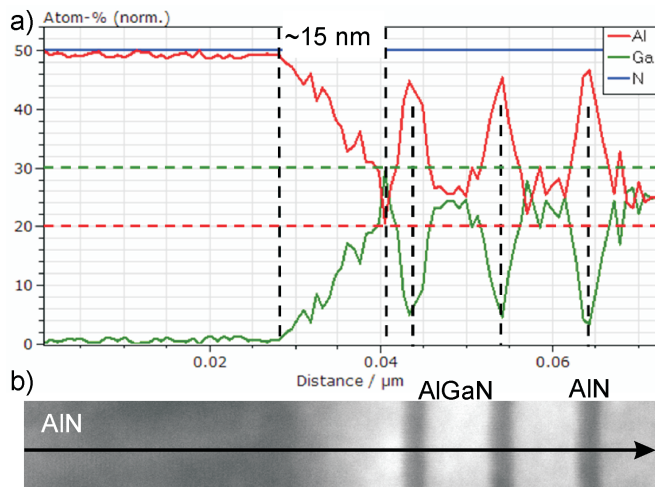
Fig. 11. a) Quantitative EDXS line scan acquired across the interface between the thick AlN buffer layer and first AlN/(Al,Ga)N superlattice layers; b) HAADF STEM image with an arrow marking the line scan direction

EDXS line scan spectra were acquired using an electron probe size of about 0.7 nm with a spatial resolution of about 0.5 nm. The dwell time of about 0.5 s per pixel and the total acquisition time of about one minute were used. The quantification of the EDX signal consisted of the following steps: i) a point EDX spectrum was obtained at the AlN buffer and the Cliff-Lorimer factor was calibrated for Al at AlN; ii) the constant N content of 50 at.% was defined; iii) the measured Al-to-Ga signal ratio and the calibrated Cliff-Lorimer coeffi-

cient for Al were used to calculate the $Al_xGa_{1-x}N$ composition. According to the measurements there is an intermixing region of about 15 nm between the AlN buffer layer and the AlN/(Al,Ga)N superlattice. The presence of the intermixing region indicates the thermal instability of (Al,Ga)N during the first deposition stages onto the AlN buffer.

In Fig. 11a the dashed horizontal lines mark the nominal concentration of the 8 nm thick $Al_{0.4}Ga_{0.6}N$ superlayers: 30 at.% of Ga and 20 at.% of Al. As visible, there is a good coincidence between the quantified data and the nominal values. It is mentionable that the quantified Al content in the 2 nm thick AlN superlayers amounts to about 45 at.%, showing only about 5 at.% error from the nominally deposited concentration.

Inversion domains are often observed in group-III wurtzite nitrides. The wurtzite crystal structure is non-centrosymmetric. There is a polar axis in the *c*-direction. Conventionally, the positive c-axis direction is chosen to point from cation (Ga, Al) to anion (N). Then, the layers grown in the [00.1] growth direction are considered to have metal polarity (e.g. Al-polarity), whereas those grown in the [00.$\bar{1}$] growth direction have N-polarity (see Fig. 12d). Nitride films grown along [00.1] and [00.$\bar{1}$] directions show different physical properties. Thus, precise control of the layer polarity during the nitride film growth is extremely important for device applications. Determination of crystal polarity is possible using X-ray photoemission spectroscopy, Rutherford backscattering and chemical etching [20]. However, these methods provide only averaged information. There are many cases where thin films do not exhibit a homogeneous polarity, but show a presence of so-called inversion domains, where the layer polarity changes locally on the scale of a few nanometers. In these cases only TEM can supply reliable results with a high spatial resolution.

In TEM the layer polarity can be analysed on the nm-scale using convergent-beam electron diffraction (CBED). In this analysis the parallel electron beam used in TEM is focused at the sample surface (converged), thus the diffraction signal is obtained only from a specimen region of a few nanometers in size. In this case the diffraction spots conventionally observed in the diffraction plane of the objective lens are expanded to diffraction discs. The diffraction technique uses the fact that in a non-centrosymmetric crystal there is a different intensity distribution within the $+g$ and $-g$ reflections along the polar axis.

As an example, Fig. 12 shows two diffraction patterns obtained from two different positions at an AlN layer grown on Al_2O_3. The CBED patterns were obtained in the [1$\bar{1}$.0] AlN zone axis. As visible from the intensity distribution in 0002 and 000-2 reflections, there is a 180°-rotation between the images. This proves the presence of inversion domains in the layers. To assign the polarity to each image it is necessary to simulate the CBED patterns. Furthermore, it is important to check if there is a 180°-rotation between the image and diffraction plane, which is present in most of the modern microscopes.
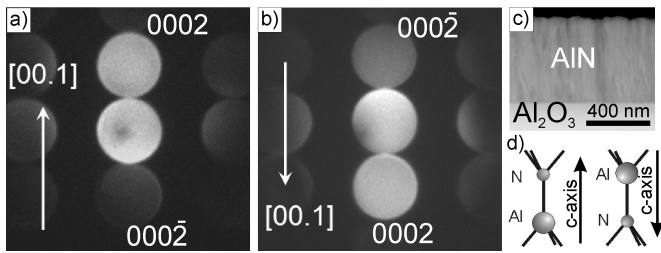
W. Neumann, H. Kirmse, I. Häusler, A. Mogilatenko, Ch. Zheng, and W. Hetaba

Fig. 12. Two experimental CBED patterns obtained in [1$\bar{1}$.0] zone axis at different specimen areas showing a) Al-polarity and b) N-polarity. Insets show the arrangement of the Al-N bilayers in the corresponding specimen areas; c) HAADF STEM image of an Al-polar AlN layer containing a large number N-polar inversion domains. Notice the high surface roughness resulting from the presence of regions with different polarities; d) Schematic arrangement of the Al-N bilayers in the Al- (left) and N-polar (right) material

CBED patterns were simulated in the [1$\bar{1}$.0] AlN zone axis for different specimen thicknesses by the software package *jems* (Fig. 13). As visible the intensity of the 0002 and 000$\bar{2}$ reflections is different allowing the polarity determination. Under kinematical diffraction conditions, i.e. at low specimen thicknesses (below one extinction distance), the intensity within the CBED disks is uniform. With increasing specimen thickness dynamic effects appear within the disks. Analysing the dynamic contrast features in CBED patterns it is possible to carry out not only the polarity determination, but also to obtain a lot of useful information on crystallography, specimen thickness, variation of the lattice plane distances, etc.
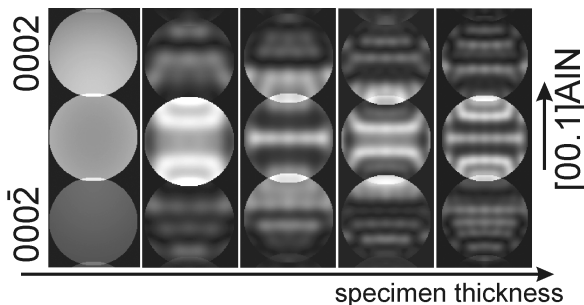

Fig. 13. CBED patterns simulated in [1$\bar{1}$.0] AlN zone axis for different specimen thicknesses

According to the simulations the grown AlN layers are Al-polar, i.e. the [00.1] AlN axis is oriented upwards (Fig. 12a, d) with N-polar inversion domains (Fig. 12b, d). It has been shown that Al-polar regions grow faster as the N-polar regions [21]. As visible in the HAADF STEM image in Fig. 12c the different growth rates result in a rough layer morphology with hills having the Al-polarity and pits of the N-polarity.

2.4. GaN/LiAlO$_2$. Since about thirty years III-nitride wide band gap semiconductors have become increasingly important due to their favourable optoelectronic properties. Unfortunately, III-nitride based optoelectronic devices have to be fabricated at foreign substrates (Al$_2$O$_3$, SiC etc.), since growth of bulk GaN single crystals is still limited to centimetre-size [22]. In

the recent years a number of research groups tested a novel γ-LiAlO$_2$ substrate with a tetragonal crystal structure for fabrication of GaN layers [23–25]. This substrate allows the growth of both polar as well as non-polar GaN layers with a low lattice mismatch. The LiAlO$_2$ substrates might be advantageous for fabrication of freestanding GaN wafers, since LiAlO$_2$ tends to a spontaneous separation from thick GaN layers during post-growth cooling down. It was shown that this separation occurs due to LiAlO$_2$ decomposition at elevated growth temperatures [26].

Figure 14 shows a cross-sectional TEM image of a thin, so-called, c-plane oriented GaN layer grown on (100) LiAlO$_2$ by hydride vapor phase epitaxy (HVPE). The GaN layers were grown along the polar [00.1] GaN direction. In the cross-sectional image of Fig. 14 the layers are viewed along the [11.0] GaN zone axis which is parallel to [001] LiAlO$_2$. A number of small crystallites (which are marked by black arrows) are observed at the GaN/LiAlO$_2$ interface.
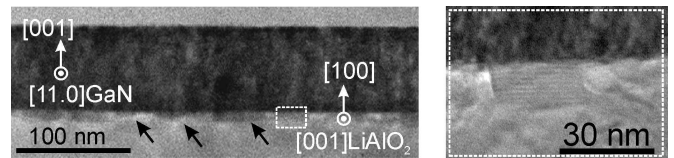

Fig. 14. Cross-sectional TEM micrograph of a GaN layer on LiAlO$_2$ substrate. A number of crystallites appearing at the GaN/LiAlO$_2$ interface are marked by arrows. An interfacial region marked by the dashed line is shown on the right at a higher magnification

Structural characterization of the interfacial crystallites has been carried out by HRTEM analysis. Figure 15 contains an image of a crystallite and its interface to the LiAlO$_2$ substrate. As visible, the high-resolution image of the crystallite reveals an ordered pattern of lattice fringes. This shows that the crystallite is epitaxially oriented to the substrate as well as to the GaN layer growing on top (not included in the image). To extract structure information the image was analyzed by a fast Fourier transform. Two regions of the micrograph were analyzed: the upper region containing the image of the interfacial crystallite with the unknown structure and the bottom region containing the image of the tetragonal LiAlO$_2$ substrate viewed in the [001] zone axis. The Fourier spectra were compared with electron diffraction simulations. First, the Fourier spectrum of the HRTEM micrograph of LiAlO$_2$ was used to calibrate the distances in the image. After that the Fourier spectrum of the HRTEM image of the unidentified crystallite was compared with electron diffraction simulations carried out for different crystal structures. Quantification of angles as well as the distances in the Fourier spectrum obtained at the interfacial crystallite showed a good agreement with the tabulated values of the cubic LiAl$_5$O$_8$ phase.

To prove this interpretation of the HRTEM images chemical characterization was carried out by EELS analysis. Figure 16 shows a set of EEL spectra acquired across the GaN/LiAlO$_2$ interfacial region together with the corresponding HAADF STEM image. The line scan direction is shown by an arrow. In the STEM image it is visible that there is

an interfacial layer consisting of crystallites which appear brighter than the LiAlO₂ substrate. This indicates a higher mean atomic number of the interfacial region. However, the HAADF STEM intensity strongly depends not only on the atomic number Z, but also on the specimen thickness. Thus considering thickness changes in the specimens (e.g. due to different ion milling rates during the specimen preparation, volume changes due to chemical reactions taking place during the layer growth, etc.) is very important.
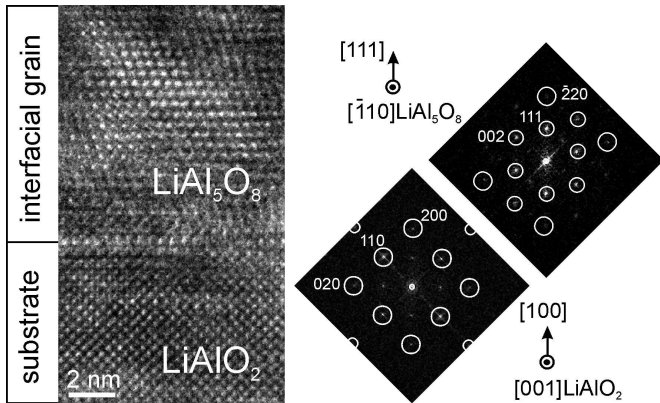

Fig. 15. HRTEM image (left) of an interfacial crystallite and its interface to the LiAlO₂ substrate. Two Fourier spectra (right) which were calculated from the substrate and the crystallite HRTEM images. Diffraction simulations (circles) correspond to the [001] LiAlO₂ zone axis (which was used for calibration of distances) and to [$\bar{1}$10] LiAl₅O₈ zone axis
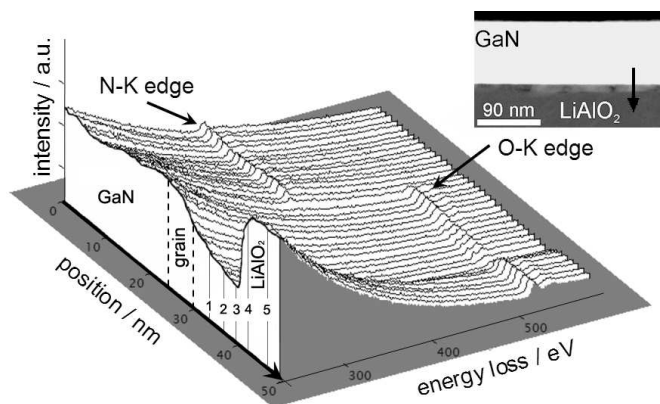
Fig. 16. STEM EELS line scan across the GaN/LiAlO₂ interface containing interfacial grains. The scan direction is shown in the inserted STEM image by an arrow. Energy loss region between 220 and 600 eV contains N-K edge at 401 eV and O-K edge at 532 eV. The numbers 1 to 5 mark positions of the spectra used for ELNES investigations discussed in Fig. 20

EEL spectra in Fig. 16 show that N-K edge is present only in the GaN region. The O-K ionization edge appears as the beam moves across the interfacial grain into the LiAlO₂ matrix. This proves the presence of oxygen in the interfacial crystallites.

EEL spectra revealing Ga distribution across the GaN/LiAlO₂ interface are shown in Fig. 17. The Ga signal was detected only in the GaN layer and not in the interfacial

grains. Unfortunately, the EELS analysis of Al as well as Li was not successful. The Al distribution can be detected using two different energy loss edges: Al-K and Al-L edge. Al-K edge appears at a high energy of 1560 eV. The intensity of the EEL spectra in this energy region is rather low. Thus, long acquisition time of typically a few seconds is required. It was observed that the interfacial grain material as well as LiAlO₂ are very sensitive to the electron irradiation and are destroyed within a few seconds of exposure to the convergent electron beam. EDXS analysis could not be used in this case for the same reason. The EDX signal in TEM is very low due to a small specimen thickness. Long acquisition time strongly improves the accuracy of measurements. But the observed material instability restricts the application of this technique.
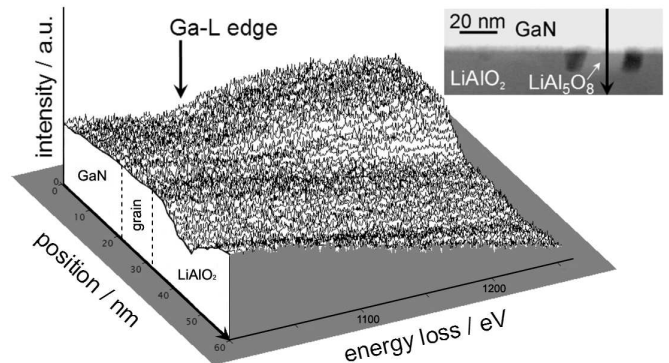

Fig. 17. STEM EELS line scan across the GaN/LiAlO₂ interface and the corresponding HAADF STEM image. The scan direction is shown by an arrow. Energy loss spectra show Ga-L edge at 1115 eV revealing the Ga distribution

On the other hand, the Al-L edge appears at a low energy of 73 eV. However, in this energy region a strong background of the plasmon peak was observed, which hindered the unambiguous EELS analysis of the Al-L edge. The strong plasmon peak background is generally caused by a large specimen thickness. It is possible to overcome this problem by preparing thinner specimens. However, it was noticed that thinner LiAlO₂ samples are faster destroyed under the electron beam. In this case low voltage TEM is required. This technique applies acceleration voltages lower than 80 kV, which allows to characterize thin beam sensitive materials, like polymers, organic nanotubes etc.

Li detection by EELS using the Li-K edge at about 55 eV is very difficult. This energy region of an EEL spectrum is dominated by a strong background of plasmon peak, which has to be properly simulated and subtracted in order to see the original Li signal. The detection of Li by EDXS is not possible, due to the absorption of low-energy X-rays in the detector window.

Background intensity of EEL spectra provides information on the specimen thickness. As visible in Fig. 16 the background intensity strongly decreases in the region of interfacial crystallites. This observation suggests that in the region of interfacial crystallites the specimen thickness is lower than in the GaN region. Furthermore, the background intensity de-

creases even more when the beam moves through the $LiAlO_2$ substrate. Then, at a certain position there is again an increase in the background level in the $LiAlO_2$ substrate region. The similar behaviour is observed in the EELS line scan revealing the Ga-L edge in Fig. 17.

This unusual behaviour of the background intensity can be explained by two independent processes. First, $LiAlO_2$ decomposition during the GaN layer growth results in a formation of interfacial $LiAl_5O_8$ crystallites, initially present in our samples. Second, the electron beam induces damaging of the $LiAlO_2$ substrate during the TEM investigations. In the following, both processes are discussed. First, the $LiAlO_2$ decomposition during the GaN layer growth is considered.

The HAADF STEM image in Fig. 17 shows that some interfacial $LiAl_5O_8$ crystallites are surrounded by regions which appear dark. In this case the lower brightness can be attributed to a smaller specimen thickness. This indicates that cavities appear around the $LiAl_5O_8$ grains. The specimen thickness at the dark regions was checked by the EELS log-ratio method. According to this method the specimen thickness can be estimated by the ratio between the zero-loss peak (ZLP) and the plasmon peak intensities [27]. In EEL spectra the ZLP has the highest intensity (Fig. 18a). It contains all elastically scattered electrons. ZLP is followed by the plasmon peak which appears as result of electron beam interaction with weakly bounded electrons in the conduction or valence band of the material. The thinner a specimen is, the more intense the ZLP and the less intense the plasmon loss is. A higher ratio corresponds to a smaller specimen thickness. Figure 18 shows the EEL spectra obtained for the dark interfacial region and $LiAlO_2$ substrate next to it. The ZLP intensity is higher and the plasmon peak intensity is lower in the dark region which indicates a lower specimen thickness. This finding confirms that the $LiAl_5O_8$ grains are partly surrounded by cavities. If the cavity alone were present under the electron beam, then the EEL spectrum would contain only the strong intensity of the direct electron beam at the ZLP position. The presence of the plasmon peak at the dark region indicates that the electron beam penetrates into the cavity and then into the $LiAlO_2$ substrate matrix behind it (Fig. 18b).
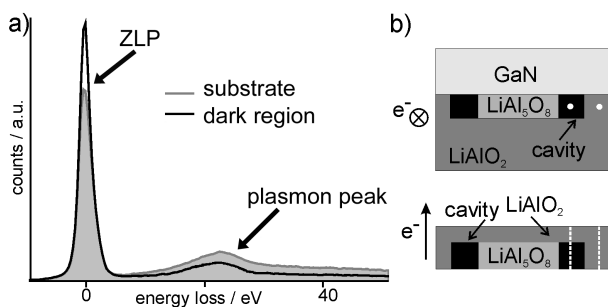
The shown results suggest that during the GaN layer growth at elevated temperatures a decomposition of $LiAlO_2$ takes place through the following reaction: $5LiAlO_2 \rightarrow 2Li_2O\uparrow + LiAl_5O_8$. The process occurs preferably at the GaN/$LiAlO_2$ interface and results in a formation of epitaxial $LiAl_5O_8$ crystallites. In this chemical reaction the volume of the consumed $LiAlO_2$ is about 1.7 times larger than the volume of the $LiAl_5O_8$ reaction product. This results in the formation of cavities around the $LiAl_5O_8$ crystallites (Fig. 17). The smaller volume and thus thickness of the $LiAl_5O_8$ crystallites explains the decreasing background intensity of the EEL spectra in the $LiAl_5O_8$ region marked as grain in Fig. 16. The release of Li and O during the GaN layer growth can be responsible for the local colouring observed in thick GaN layers grown on $LiAlO_2$ [28]. Furthermore, the formation of such porous interface is responsible for the spontaneous separation of $LiAlO_2$ substrates from thick GaN layers [23].

As has been mentioned above, $LiAlO_2$ is extremely unstable under the electron beam irradiation during TEM observations. Understanding of this behaviour is extremely important to avoid misleading interpretation of results. To monitor the changes in γ-$LiAlO_2$ substrates energy-loss near edge structure (ELNES) of O-K edge has been analyzed.

ELNES is a powerful tool for chemical composition analysis and distinguishing of the bonding character of materials on the nanometer scale. In particular, ELNES provides information on the distribution of unoccupied electronic states. Thus, the shape of ELNES is extremely sensitive to the local environment of atoms and thus to their coordination, valence state and bonding type. This allows quantitative characterization of materials containing the same chemical elements but present in the different atomic modifications.

Figure 19 shows an evolution of the O-K edge shape during STEM investigations compared with the corresponding ELNES simulations which were carried out using the full potential augmented plane wave code WIEN97 [29] which is based on the density functional theory. The experimental results were obtained at a strongly focused electron beam of about 1 nm in diameter and an acceleration voltage of 200 kV. During the experiment the electron beam was kept stationary at a given specimen position.
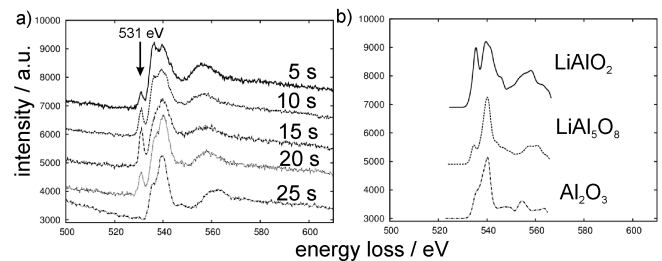

Fig. 18. Geometry of $LiAl_5O_8$ grains: a) Low-loss spectrum region containing information on elastically scattered electrons and the plasmon losses. A higher ZLP-to-plasmon intensity ratio in the dark region corresponds to a smaller specimen thickness. b) Sketches of the sample structure visualizing the electron beam position used for the measurements shown in (a): cross-sectional view (top) and top-view without the GaN layer (bottom)

Fig. 19. Time-resolved ELNES of γ-$LiAlO_2$: a) Experimental O-K edge spectra acquired at a focused electron beam of 1 nm in diameter at 200 kV accelerating voltage at different irradiation time; b) simulated ELNES of O-K edge for different phases

In Fig. 19a it is visible that the shape of the O-K edge changes with time. The ELNES simulations (Fig. 19b) suggest

248

transformation of $LiAlO_2$ into $LiAl_5O_8$ and subsequently into Al_2O_3 during the STEM analysis. Furthermore, the comparison of the experimental peaks with the ELNES simulations of different $Li_xAl_yO_z$ compounds reveals the presence of an additional peak at 531 eV in some experimental spectra. Its intensity changes with observation time: there is an increase of the peak intensity at the beginning (from 5 s to 15 s) followed by a strong decline until the peak completely disappears (from 20 s to 25 s). This peak can be associated with the presence of molecular oxygen at the sample surface.

The EELS observations suggest the following electron beam induced changes in $LiAlO_2$. First, O_2 and probably Li escape out of $LiAlO_2$ matrix which results in an Al-rich local environment around the focused beam. As a result, the chemical composition of the material changes according to the following scheme: $LiAlO_2 \rightarrow LiAl_5O_8 \rightarrow Al_2O_3$. As soon as Al_2O_3 is formed the transformation is completed, since this phase is stable under electron irradiation. Consequently, the additional O_2 peak intensity at 531 eV falls rapidly down.

Unfortunately, up to now it is not clear in which form Li escapes out of $LiAlO_2$. There are a number of possible Li-based gaseous compounds: Li, LiO, Li_2O and Li_2O_2. Thus, ELNES investigations of the Li edge would complete this decomposition scenario. For example, it has been shown that the Li K-edge ELNES strongly differs for Li and Li_2O [30]. However, for the analysis of Li K-edge ELNES a monochromatic electron beam is required. This investigation is still in process.

It should be mentioned that the short transformation time shown in Fig. 19a can be reached only for a sharply focused electron beam. The duration strongly depends on the beam current density and the specimen thickness. In conventional TEM analysis using a parallel beam illumination with much lower current densities the $LiAlO_2$ transformation time can be drastically decreased.

After analysing the $LiAlO_2$ decomposition scenario caused by the electron beam in TEM the following explanation of changes in the EELS background intensity visible in the $LiAlO_2$ substrate region in Fig. 16 and 17 can be proposed. Figure 20 shows five spectra extracted from the EELS line scan according to the numbering marked in Fig. 16. Notice that all spectra were obtained at the $LiAlO_2$ substrate. In Fig. 20 they are ordered according to their position from the film/$LiAlO_2$ interface and not according to their absolute intensity. For changes of background intensity see Fig. 16. Obviously, as soon as the electron beam starts moving across the $LiAlO_2$ the transformation of the local environment of the beam cross-section begins. First stages of development of the $LiAlO_2$ transformation can be tracked in spectra from 1 to 3. In coincidence with the above described electron beam induced $LiAlO_2$ transformation there is an increasing intensity of the peak associated with the molecular oxygen released from the substrate. At very thin $LiAlO_2$ regions (close to the GaN/$LiAlO_2$ interface) the transformation is very fast, so that a complete destruction of material up to drilling holes through the whole sample was occasionally observed. This explains a very rapid decrease of the EELS background in-

tensity in $LiAlO_2$ spectra visible in Fig. 16 (for positions 1 to 3). When the transformation has been completed and Al_2O_3 has been formed the EELS background intensity recovers and stays approximately the same indicating the formation of a stable phase with an almost unchanged thickness (Fig. 16 positions 4 to 5). The Al_2O_3 formation can be recognized from the shape of the O-K edge in the spectra 4 and 5 of Fig. 20 (compare to the simulation carried out for Al_2O_3 and shown in Fig. 19b).
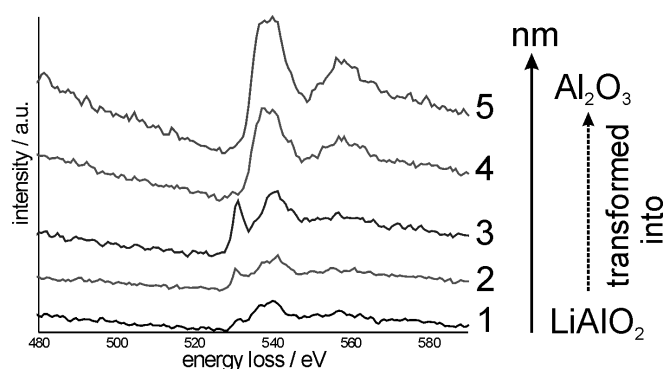

Fig. 20. ELNES of the O-K edge extracted from the EELS line scan (shown in Fig. 16) carried out through a $LiAlO_2$ region. The spectra numbering corresponds to the notations marked in Fig. 16

2.5. FeCo-based soft-magnetic nanocrystalline alloys. The magnetic domain structure is an important feature of ferromagnetic materials. It directly reflects the magnitude and anisotropy of the microscopic exchange interaction [31]. It is well known that magnetic domain configurations as well as their shape and size strongly depend on the microstructure of the material. For technical applications it is possible to improve the magnetic properties by optimizing the structure of materials. Such optimisation requires a detailed understanding of the correlations between microstructure and magnetic domain structure on the scale of the exchange length, which is normally a nanometer scale [32].

FeCo-based nanocrystalline soft magnetic alloys of the following nominal composition $(Fe_{0.5}Co_{0.5})_{80}Nb_4B_{13}Ge_2Cu_1$ were prepared by melt spinning and a subsequent annealing procedure (500°C, 1 h) to transform the amorphous alloy into a nanocrystalline phase. This material is a promising candidate material for high temperature and power conversion application [33]. Investigations of the structure of the alloy were carried out by means of conventional TEM and HRTEM. The formed alloy is a two-phase structure consisting of crystalline α-FeCo randomly oriented particles (bcc structure) with an average grain size of ~ 12 nm embedded in the residual amorphous matrix as shown in Fig. 21.

The magnetic properties of the FeCo-based alloy were investigated by Lorentz microscopy and electron holography. These techniques are particularly useful for studying soft-magnetic materials which can be easily magnetized or demagnetized even in a weak applied field.
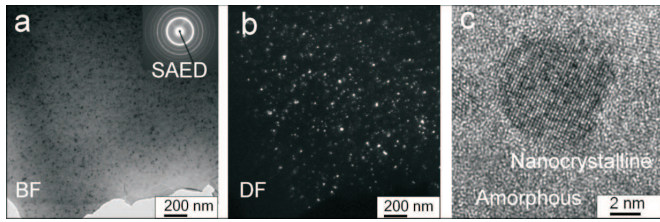
W. Neumann, H. Kirmse, I. Häusler, A. Mogilatenko, Ch. Zheng, and W. Hetaba

Fig. 21. Microstructure of $(Fe_{0.5}Co_{0.5})_{80}Nb_4B_{13}Ge_2Cu_1$ nanocrystalline soft-magnetic alloy: (a) bright-field TEM image (inserted: diffraction pattern); (b) dark-field TEM image; (c) HRTEM image

Both, Lorentz microscopy and electron holography investigations were performed in the Lorentz mode. In this mode the normal objective lens is switched off and the focus function is taken over by an objective mini lens below the lower pole piece of the objective lens. Then the sample is located at a field-free environment and the natural magnetizations inside the sample are preserved during the investigation. Otherwise the magnetic domain structures will be destroyed since the strong field of the objective lens field will align all of the magnetizations inside the sample along the optical axis. Since the objective lens is switched off the resolution in the Lorentz mode is lower as in conventional TEM and the magnification is limited. The difference between the conventional TEM mode and Lorentz mode is schematically illustrated in Fig. 22.
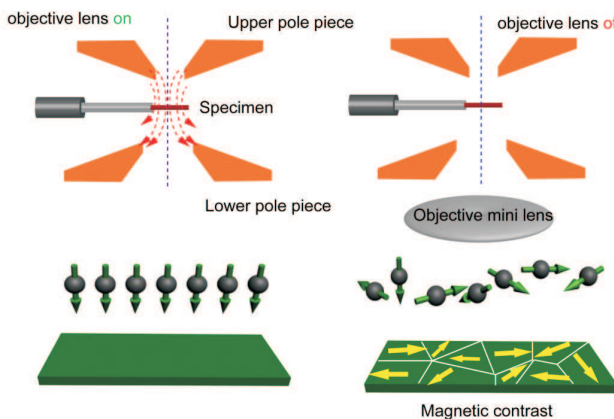

Fig. 22. Two different working modes in TEM. Left: conventional TEM mode for structure imaging. Right: Lorentz mode for magnetic structure imaging

The formation of magnetic contrast in Fresnel mode Lorentz microscopy is illustrated in Fig. 23. When incident electrons interact with the magnetic sample, they will be deflected by Lorentz force and the deflection directions are determined by Fleming's left hand rule. The magnetization direction varies from domain to domain. When electrons transmit through two adjacent $180°$ domains, they will be deflected towards opposite directions. Subsequently, the convergent or divergent electrons at the positions of domain walls will form black or dark contrast under the bottom surface of the sample [16]. Such magnetic contrast can then be observed under large defocus conditions, as shown in Fig. 23.
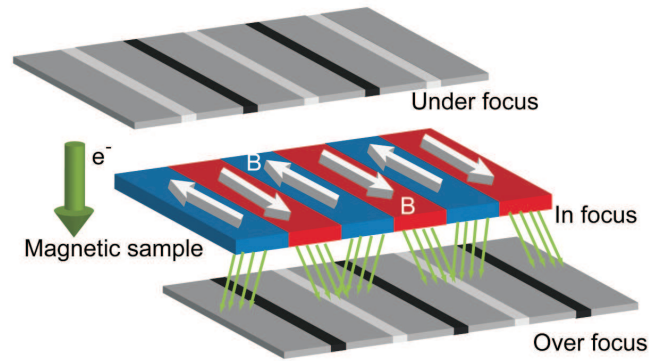

Fig. 23. Formation of magnetic contrast in the Fresnel mode of Lorentz microscopy

A series of Lorentz microscopy images observed in the Fresnel mode of the as-prepared FeCo-based alloys is shown in Fig. 24. The in-focus image in Fig. 24a looks like a conventional bright-field image and shows only structure contrast. In the strongly defocused Lorentz microscopy images (Fig. 24b and c, $\Delta f = \pm 1536$ μm), black and dark lines clearly indicate the locations of domain walls. The size of the domains ranges from several hundred nanometers to more than one micrometer, which is much larger than the average size of FeCo grains. This hints to good soft-magnetic properties of the sample.
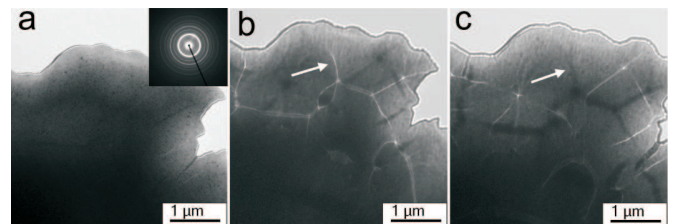

Fig. 24. Series of Lorentz microscopy images of FeCo-based alloys. a) in focus; b) overfocused; c) underfocused. The positions of domain walls are visualized as black and dark lines (see arrows)

In order to get more detailed information about the magnetic flux distributions within the sample, electron holography was further applied. Different from conventional TEM, both the amplitude and phase of electrons exit wave are recorded by electron holography [2].

A simple illustration of the formation of an electron hologram in TEM is presented in Fig. 25. In order to record the phase shift of electrons, an electrostatic biprism is inserted close to the first imaging plane. When a positive voltage is applied to the biprism, an electrostatic field will be created around it and deflect the object wave and the reference wave (transmitted through the vacuum) towards each other. In the image plane interference fringes will be formed and then further magnified by the successive lens system. Finally, the interference patterns are recorded by a CCD camera as an electron hologram.

Thus, the complete information of object wave φ_{obj}, including both the amplitude and the phase are recorded in the hologram. By using digital Fourier transform reconstruction

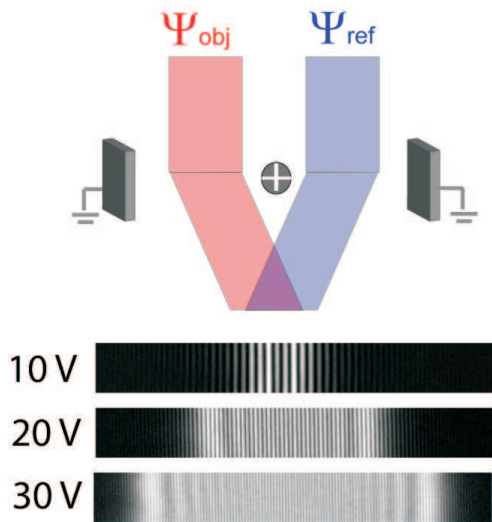technique the amplitude and phase information will be further extracted from the hologram.

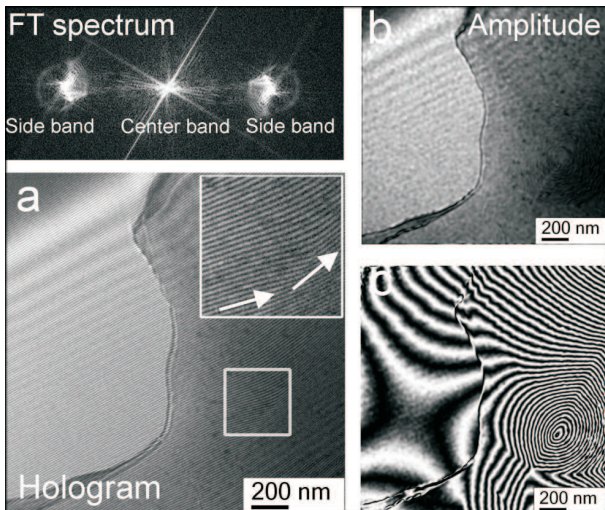Fig. 25. Basic principle of off-axis electron holography

Fig. 26. Electron holography of the as-grown FeCo-based alloy: a) Electron hologram; b) Reconstructed amplitude and c) phase images of FeCo-based alloys. The phase image has been amplified by two times

Figure 26 shows a typical electron hologram, the reconstructed amplitude and phase image of the as-prepared FeCo-based nanocrystalline alloy. The vacuum in the left part of the hologram is used for transmission of reference wave. An enlarged part of the hologram inserted at the upper right (Fig. 26a) clearly shows that the fringes which reflect the information about the phase shift of the electrons are strongly distorted across the sample due to the effects of magnetic vector potential. The phase shift can be recognised more easily from the Fourier transform spectrum of the hologram (at the top of Fig. 26a). Instead of single spots the side bands are strongly dispersed. The amplitude image reconstructed from the hologram is presented in Fig. 26b, it looks similiar to a conventional BF-TEM image without any special magnetic

contrast. Contrary to that, the phase image (Fig. 26c) shows a distinct feature, namely large black and white contour lines. The spacing between two adjacent contour lines corresponds to a phase shift of π (amplified two times from the reconstructed raw phase image). Since the ion-milling prepared sample has a slowly varied thickness, the contribution of mean inner potential to the phase gradient can be neglected. Thus, the contour lines directly visualize the magnetic flux distributions in and around the sample. Some leakage field is observed in the vacuum close to the edge of the sample, while inside the sample, a closure structure is clearly visible. This indicates that the alloy has a low magneto-crystalline anisotropy.

In order to better visualize the magnetic domain structures the directions of magnetic flux were further calculated from the phase image. This is performed by calculating the directions of the phase gradient and further rotating by $90°$. The colour coded mapping of magnetic flux directions is shown in Fig. 27. It reveals that the closure structure is actually formed by four adjacent domains.
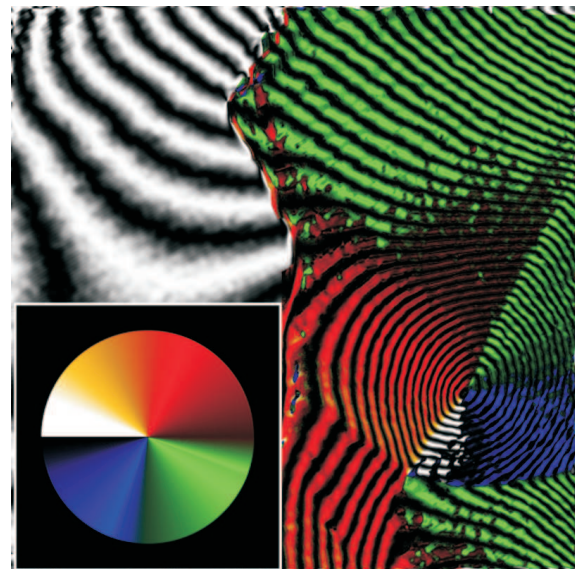

Fig. 27. Colour-coded magnetic flux distribution in FeCo-based soft-magnetic alloys. The directions of magnetic flux are indicated by the colour-wheel inserted at bottom left. Image size: $1.82 \, \mu m \times 1.82 \, \mu m$

To determine the width of magnetic domain walls, a phase line profile perpendicular to a $180°$ magnetic domain wall is plotted in Fig. 28. The phase jump has been previously removed by the phase unwrap processing. The curve clearly shows three distinguished parts. On the left hand side the phase gradient linearly increases while on the right hand side the sign of the phase gradient is reversed. This indicates that the magnetization directions in the adjacent $180°$ magnetic domains are opposite to each other. In the central region the slope of the curve is approximately flat. This reveals that the magnetizations in such region are rotated with respect to the directions of adjacent two domains. So this part corresponds to the region of magnetic domain wall. The measured width of the wall amounts to 32.1 nm. Since the average FeCo grain size ($\sim$ 12 nm) is much smaller than the width of domain wall

(or exchange length) determined here, it reveals that the effective magneto-crystalline anisotropy can be significantly reduced by exchange interaction over several randomly oriented grains. This clearly explains the origin of the good soft magnetic properties in such kind of nanocrystalline alloys [34].
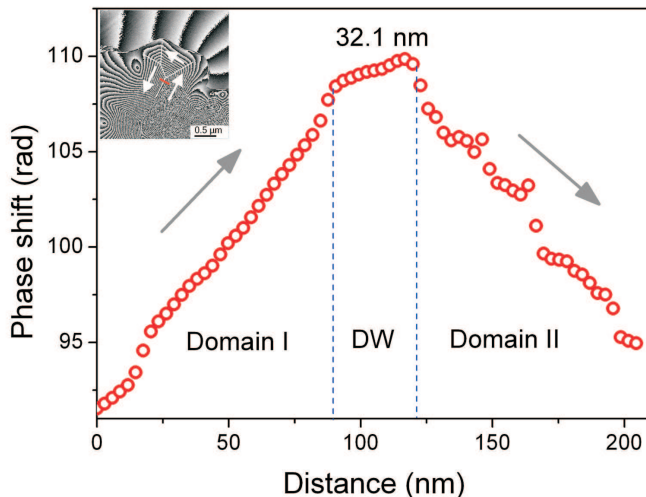

Fig. 28. Unwrapped phase line profile perpendicular to a 180° domain wall. The relatively flat part in the center region clearly reveals the width of domain wall

3. Conclusions and outlook

We have demonstrated how the various methods of TEM can succesfully be applied to analyse the structure and chemical composition of materials. In conjunction with the development of the instrumental technique in TEM a further development and application of both the analytical techniques and the interpretation methods as a function of dimensionality of the materials is essential.

Within the last decade the revolutionary instrumental development in electron microscopy has led to the availability of aberration-corrected TEMs and STEMs [35, 36]. First results of aberration-corrected TEM in materials science obtained within the world-wide first spherical aberration C_s-corrected TEM were published in 1998 [37]. Meanwhile various commercial microscopes are/ or can be optionally equipped with objective lens and/or electron probe correctors (e.g.,TEM/STEMs: FEI Titan, JEOL JEM2200 FS, JEM – ARM200F, dedicated STEMs: Nion UltraSTEM 100 and 200, HITACHI HD-2700). State of the art instruments were developed in the TEAM (Transmission Electron Aberration-corrected Microscope) project, where the microscopes TEAM 0.5 and TEAM I were delivered [38]. The TEAM 0.5 microscope is equipped with a monochromated field emission gun, has two CEOS hexapole correctors for the objective lens and the electron probe and a GATAN GIF Tridiem energy-filter. The instrument is capable to obtain a spatial resolution of 0.5 Å in TEM and STEM. TEAM I as the final instrument is additionally equipped with a prototype of an optical system correcting both the spherical (C_s) and the chromatic (C_c) aberration. First results of the potential of

chromatic aberration for HRTEM and EFTEM have been recently published [39]. In general, the aberration correction has not only drastically improved the image resolution. The aberration correction, together with the use of a monochromated beam has led significant improvements in EELS, EFTEM and also in EDXS.

Future trends in aberration-corrected electron microscopy are related to the development of low-voltage aberration corrected phase TEM using a coma-free objective lens, a phase plate and a novel C_s/C_c-corrector within the SALVE project (**S**ub-Å **L**ow **V**oltage **E**lectron microscope) [40].

Within the forthcoming years the aberration correction microscopy will open new fields and dimensions of materials analysis. This will also include the important area of dynamic realtime in-situ studies in TEM [41].

REFERENCES

[1] I. Häusler, H. Kirmse, and W. Neumann, "Composition analysis of ternary semiconductors by combined application of conventional TEM and HRTEM", *Phys. Stat. Sol.* A 205, 2598–2602 (2008).

[2] H. Lichte, P. Formanek, A. Lenk, M. Linck, Ch. Matzeck, M. Lehmann, and P. Simon, "Electron holography: Applications to materials questions", *Annu. Rev. Mater. Res.* 37, 539–588 (2007).

[3] W. Coene, A. Thust, M. Op de Beeck, and D. Van Dyck, "Maximum-likelihood method for focus-variation image reconstruction in high-resolution electron microscopy", *Ultramicroscopy* 64, 109–135 (1996).

[4] S. Kret, P. Ruterana, A. Rosenauer, and D. Gerthsen, "Extracting quantitative information from high resolution electron microscopy", *Phys. Stat. Sol* B 227, 247–295 (2001).

[5] R.J. Vincent and P.A. Midgley, "Double conical beam-rocking system for measurement of integrated electron diffraction intensities", *Ultramicroscopy* 53, 271–282 (1994).

[6] M. Tanaka; R. Saito, K. Ueno, and Y. Harada, "Large-angle convergent-beam electron diffraction", *J. Electron Microsc.* 29, 408–412 (1980).

[7] J.P. Morniroli, "CBED and LACBED characterization of crystal defects", *J. Microsc.* 223, 240–245 (2006).

[8] D.A. Muller, L. F. Kourkoutis, M. Murfitt, J.H. Song, H.Y. Hwong, J. Silcox, N. Dellby, and O.L. Krivanek, "Atomic-scale chemical imaging of composition and bonding

by aberration-corrected microscopy", *Science* 319, 1073-1076 (2008).

[9] A.K. Petford-Long and J. M. Chapman, "Lorentz microscopy", in: *Magnetic microscopy of nanostructures*, eds. H. Hopster, H.P. Oepen, pp. 67–86, Springer, New York, 2005.

[10] M. Lehmann and H. Lichte, "Electron holographic material analysis at atomic dimensions", *Crystal Research and Technology* 40, 149–160 (2005).

[11] P.A. Midgley and M. Weyland, "3D electron microscopy in the physical sciences: the development of Z-contrast and EFTEM tomography", *Ultramicroscopy* 96, 413–431 (2003).

[12] G. Schumacher, N. Darowski, I. Zizak, H. Klingelhöffer, W. Chen, and W. Neumann, "Temperature dependence of lattice distortion in strongly creep-deformed single crystal superalloy SC16", *Materials Science Forum* 539–543, 3048–3052 (2007).

[13] A. Rosenauer, U. Fischer, D. Gerthsen, and A. Förster, "Composition evaluation by lattice fringe analysis", *Ultramicroscopy* 72, 121 (1998).

[14] S. Blumstengel, N. Koch, S. Sadofev, P. Schäfer, H. Glowatzki, R.L. Johnson, J.P. Rabe, and F. Henneberger, "Interface formation and electronic structure of sexithiophene on ZnO", *Appl. Phys. Lett.* 92, 193303 (2008).

[15] V. Srikant, J.S. Speck, and D. R. Clarke, "Mosaic structure in epitaxial thin films having large lattice mismatch", *J. Appl. Phys.* 82, 4286–4295 (1997).

[16] P. Hirsch, A. Howie, R. Nicholson, D.W. Pashley and M.J. Whelan, "Electron microscopy of thin crystals", *Library of Congress Cataloging in Publication Data* 1, 176–185 (1977).

[17] O. Reentilä, F. Brunner, A. Knauer, A. Mogilatenko, W. Neumann, H. Protzmann, M. Heuken, M. Kneissl, M. Weyers, and G. Tränkle, "Effect of the AlN nucleation layer growth on AlN material quality", *J. Cryst. Growth.* 310, 4932–4934 (2008).

[18] D. Hull and D.J. Bacon, "Introduction to dislocations", *Int. Series on Materials Science and Technology* 37, 114–115 (1984).

[19] C. Stampfl and C.G. Van de Walle, "Energetics and electronic structure of stacking faults in AlN, GaN, and InN", *Phys. Rev. B* 57, 52–55 (1998).

[20] E.S. Hellman, "The polarity of GaN: a critical review", *MRS Internet J. Nitride Res.* 3, 1–11 (1998).

[21] J. Jasinski, Z. Liliental-Weber, Q.S. Paduano, and D.W. Weyburne, "Inversion domains in AlN grown on (0001) sapphire", *Appl. Phys. Lett.* 83, 2811–2813 (2003).

[22] I. Grzegory, B. Lucznik, M. Bockowski, and S. Porowski, "Crystallization of low dislocation density GaN by high-pressure solution and HVPE methods", *J. Cryst. Growth* 300, 17–25 (2007).

[23] H.P. Maruska, D.W. Hill, M.C. Chou, J.J. Gallagher, and B.H. Chai, "Free-standing non-polar gallium nitride substrates", *Opto-Electronics Rev.* 11, 7–17 (2003).

[24] E. Richter, Ch. Hennig, U. Zeimer, M. Weyers, G. Tränkle, P. Reiche, S. Ganschow, R. Uecker, and K. Peters, "Freestanding two-inch c-plane GaN layers grown on (100) γ–lithium aluminium oxide by hydride vapour phase epitaxy", *Phys. Stat. Sol.* C 3, 1439–1443 (2006).

[25] Z. Liliental-Weber, J. Jasinski, and D.N. Zakharov, "GaN growth in polar and non-polar direction", *Opto-Electronics Rev.* 12 (4), 339–346 (2004).

[26] A. Mogilatenko, W. Neumann, E. Richter, M. Weyers, B. Velickov, and R. Uecker, "Mechanism of LiAlO$_2$ decomposition during the GaN growth on (100) γ-LiAlO$_2$", *J. Appl. Phys.* 102, 023519 (2007).

[27] J. Hosoi, T. Oikawa, M. Inoue, Y. Kokubo, and K. Hama, "Measurement of partial specific thickness (net thickness) of critical-point-dried cultured fibroblast by energy analysis", *Ultramicrocopy* 7, 147–153 (1981).

[28] A. Mogilatenko, W. Neumann, E. Richter, M. Weyers, B. Velickov, and R. Uecker, "TEM study of c-plane layers grown on γ-LiAlO$_2$(100)", *Phys. Stat. Sol.* C 5, 3712–3715 (2008).

[29] P. Blaha, K. Schwarz, P. Sorantin, and S.B. Trickey, "Full-potential, linearized augmented plane wave programs for crystalline systems", *Comput. Phys. Commun.* 59, 399–415 (1990).

[30] V. Mauchamp, F. Boucher, G. Ouvrard, and P. Moreau, "Ab initio simulation of the electron energy-loss near-edge structures at the Li K edge in Li, Li$_2$O, and LiMn$_2$O$_4$", *Phys. Rev. B* 74, 115106 (2006).

[31] T. Shono, T. Hasegawa, T. Fukumura, F. Matsukura, and H. Ohno, "Observation of magnetic domain structure in a ferromagnetic semiconductor (Ga, Mn)As with a scanning Hall probe microscope", *Appl. Phys. Lett.* 77 (9), 1363–1365 (2000).

[32] D. Jiles, *Introduction to Magnetism and Magnetic Materials*, CRC Press, New York, 1998.

[33] M. McHenry, M. Willard, and D. Laughlin, "Amorphous and nanocrystalline materials for applications as soft magnets", *Progress in Materials Science* 44 (4), 291–433 (1999).

[34] G. Herzer, "Soft magnetic nanocrystalline materials", *Scripta Metallurgica et Materiala* 33 (10–11), 1741–1756 (1995).

[35] H. Rose, "Historical aspects of aberration correction", *J. Electron Microsc.* 58 (3), 77–85 (2009).

[36] D.J. Smith, "Development of aberration-corrected electron microscopy", *Microscopy and Microanalysis* 14, 2–15 (2008).

[37] M. Haider, H. Rose, S. Uhlemann, E. Schwan, B. Kabius, and K. Urban, "Towards 0.1 nm resolution with the first spherically corrected transmission electron microscope", *J. Electron Microsc.* 47, 395–405 (1998).

[38] U. Dahmen, R. Erni, V. Radmilovic, C. Kisielowski, M.D. Rossell, and P. Denes, "Background, status and future of the transmission electron aberration-corrected microscope project", *Phil. Trans. R. Soc.* A 367, 3795–3808 (2009).

[39] B. Kabius, P. Hartel, M. Haider, H. Müller, St. Uhlemann, U. Loebau, J. Zach, and H. Rose, "First application of C$_c$-corrected imaging for high-resolution and energy-filtered TEM", *J. Electron Micr.* 1–9, doi:10.1093/jmicro/dfp021 (2009).

[40] U. Kaiser, A. Chuvilin, J. Meyer, and J. Biskupek, "Microscopy at the bottom", *Proc. MC2009, Microscopy Conf.* 3, 1–6 (2009).

[41] Th. LaGrange, G.H. Campbell, B.W. Reed, M. Taheri, J. Bradley Pesavento, J.S. Kim, and N.D. Browning, "Nanosecond time-resolved investigations using in situ of dynamic transmission electron microscope (DTEM)", *Ultramicroscopy* 108, 1441–1449 (2008).